THE ASTROPHYSICAL JOURNAL, 465:425–435, 1996 July 1

J. K. LAWRENCE, A. C. CADAVID, AND A. A. RUZMAIKIN
Department of Physics and Astronomy, California State University, Northridge, Northridge, CA 91330-8268
Received 1995 September 7; accepted 1996 January 16

ABSTRACT

Many studies have pointed out fractal and multifractal properties of photospheric magnetic fields, but placing the various approaches into context has proved difficult. Although fractal quantities are defined mathematically in the asymptotic limit of infinite resolution, real data cannot approach this limit. Instead, one must compute fractal dimensions or multifractal spectra within a limited range at finite scales. The consequent effects of this are explored by calculation of fractal quantities in finite images generated from analytically known measures and also from solar data. We find that theorems relating asymptotic quantities need not hold for their finite couterparts, that different definitions of fractal dimension that merge asymptotically give different values at finite scales, and that apparently elementary calculations of dimensions of simple fractals can lead to incorrect results. We examine the limits of accuracy of multifractal spectra from finite data and point out that a recent criticism of one approach to such problems is incorrect.

Subject headings: methods: analytical — methods: numerical — Sun: magnetic fields

1. INTRODUCTION

Magnetic flux in the solar photosphere is intermittently structured down to the smallest scales accessible to terrestrial instruments. This manifests itself in a scale similarity of the distribution of magnetic areas on the solar surface and a corresponding fractal dimension $D \approx 1.6$ (Tarbell et al. 1990). Because the solar magnetic flux density is not uniform, one must define a measure on the fractal set. Measure theoretical concepts were first applied to solar fields by Lawrence, Ruzmaikin, & Cadavid (1993), who found that the solar flux also is multifractal. Subsequently, small-scale dynamo models have been proposed to produce multifractal fields and have been tested against observational data (Cadavid et al. 1994; Lawrence, Cadavid, & Ruzmaikin 1995a).

The application of fractal and multifractal methods to solar problems is becoming increasingly common (Brandt et al. 1991; Lawrence 1991; Ruzmaikin, Sokoloff, & Tarbell 1991; Schrijver et al. 1992; Lawrence & Schrijver 1993; Milovanov & Zelenyi 1993; Lawrence et al. 1995b; Tao et al. 1995). These works approach fractality and multifractality from a variety of viewpoints and may, at times, appear contradictory. A reconciliation of some of these results is timely. It is also appropriate to illustrate pitfalls, both computational and interpretive, which investigators may encounter.

Fractal dimensions and multifractal spectra are defined mathematically in the asymptotic limit of infinite resolution and hence over an infinite range of scales. No set of observational or simulated data can approach this limit. All are bounded by an inner cutoff at finite resolution and by an outer cutoff at the scale of the system under observation (or simply of the image size). One is left with a scaling range somewhere between the two cutoffs. We will use the term "resolution-limited asymptotics" to describe this situation. When asymptotic and resolution-limited asymptotic quantities are confused, theorems relating mathematical quantities may appear to be violated, and apparently straightforward computations can lead to incorrect answers. Different definitions of fractal dimension that coincide asymptotically often yield markedly different values when calculated from data. Dubuc et al. (1989) have remarked on the weakness of box counting methods for studying fractal dimensions of graphs of finite time series. Scotti, Meneveau, & Saddoughi (1995) have given a thorough analysis of the scaling corrections needed for calculation of fractal dimensions of such graphs. Their findings parallel, in some aspects, our results for magnetic images. Finally, different kinds of fractal dimensions can be computed for the same sets or measures, leading to inappropriate comparisons of calculated values.

We will illuminate these problems by analyzing, in the context of resolution-limited asymptotics, artificial images with known asymptotic properties and comparing the results to mathematical expectations. Each case will be illustrated by an example from solar data.

2. MULTIFRACTAL MEASURES

Let us cover an image of the solar surface, including magnetic flux, with a grid of square "coarse-graining" cells or boxes of uniform sizes $s = \epsilon L$, where L is an outer cutoff scale, and where $\epsilon \ll 1$. Then we define a measure μ, on the set of boxes containing magnetic flux, that describes the variation of the flux, or other measure, from box to box. For finite ϵ, the coarse-grained measure $\mu_i(\epsilon)$ in the ith box is the integral of the measure μ over that box. If the measure is signed, as for line-of-sight flux (Lawrence et al. 1993; Cadavid et al. 1994), the opposite signed components cancel within each box, and then the absolute value is taken. If the frequency distribution of the measure among the boxes is invariant as ϵ is varied, then it is multifractal (Evertsz & Mandelbrot 1992).

A fixed coarse-graining grid is useful for conceptual purposes, but for large ϵ's there are not enough boxes for good counting statistics. Further, results can be distorted by fortuitous alignment of the grid with image features. In computations we will place Monte Carlo sampling boxes randomly in the image.

2.1. *Multiplicatively Generated Multifractals*

We explore finite size effects by examination of a known measure generated by a multiplicative cascade process. This

is a restricted version of the two-dimensional procedure used by Lawrence et al. (1995a). A measure uniformly distributed on a square area is divided among four equal quarters according to two multipliers M_1 and M_2, selected at random from the same distribution density $P(M) = P(1 - M)$, where $0 \leq M \leq 1$. The four subsquares are allocated the measures M_1M_2, $M_1(1 - M_2)$, $(1 - M_1)M_2$, and $(1 - M_1)(1 - M_2)$, respectively. Then, the four squares are further divided into four equal quarters according to the same procedure and with the same probability density, and so on to infinity. The invariance of the allocation rule through all the levels of subdividion produces multifractal scaling. Figure 1 is a gray-scale image of a 512 pixels × 512 pixels image constructed from the first nine steps of such a procedure with a triangular distribution density: $P(M) = 4M$ for $0 \leq M \leq \frac{1}{2}$ and $P(M) = 4(1 - M)$ for $\frac{1}{2} \leq M \leq 1$.

2.2. *Generalized Dimensions*

The asymptotic limit of the qth moment of the measure gives the "generalized dimensions"

$$D_q = \frac{1}{(q-1)} \lim_{\epsilon \to 0} \frac{\ln \sum_i \mu_i^q(\epsilon)}{\ln \epsilon}, \tag{2.1}$$

where q is any real number (Grassberger 1983; Hentschel & Procaccia 1983; Halsey et al. 1986). D_0 is just the fractal dimension of the supporting set of the measure. The generalized dimensions are a nonincreasing function of q (Hentschel & Procaccia 1983). The measure of a simple fractal is uniform, so $D_q = D$ for all q. The limit $q \to 1$ exists:

$$D_1 = \lim_{\epsilon \to 0} \frac{-\sum_i \mu_i \ln \mu_i}{\ln (1/\epsilon)}. \tag{2.2}$$

The "measure theoretic" dimension D_1 describes the concentration of the measure. For example, when D_0 describes the distribution of a set of coins, D_1 describes the distribution of their monetary value (measure).

In the resolution-limited asymptotics of real data, we remove the limits from equations (2.1) and (2.2), write

$$\sum_i \mu_i^q(\epsilon) \propto \epsilon^{(q-1)D_q}, \tag{2.3}$$

and find D_q by a linear fit of $\ln [\sum_i \mu_i^q(\epsilon)]$ to $\ln (1/\epsilon)$. The intercept $C(q)$ of the fit indicates the importance of finite-size effects.

As a result of its scale invariance, the moments of the measure of Figure 1 can be reduced to the moments of $P(M)$:

$$\langle M^q \rangle = \int_0^1 dM P(M) M^q = \frac{4}{(q+1)(q+2)} \left[1 - \left(\frac{1}{2} \right)^{q+1} \right] \tag{2.4}$$

if $q > -2$ and $q \neq -1$, and

$$\langle M^{-1} \rangle = 4 \ln 2. \tag{2.5}$$

$\langle M^q \rangle$ is singular for $q \leq -2$ because of the M^{q+1} dependence of the integrand at $M \sim 0$. The generalized dimen-

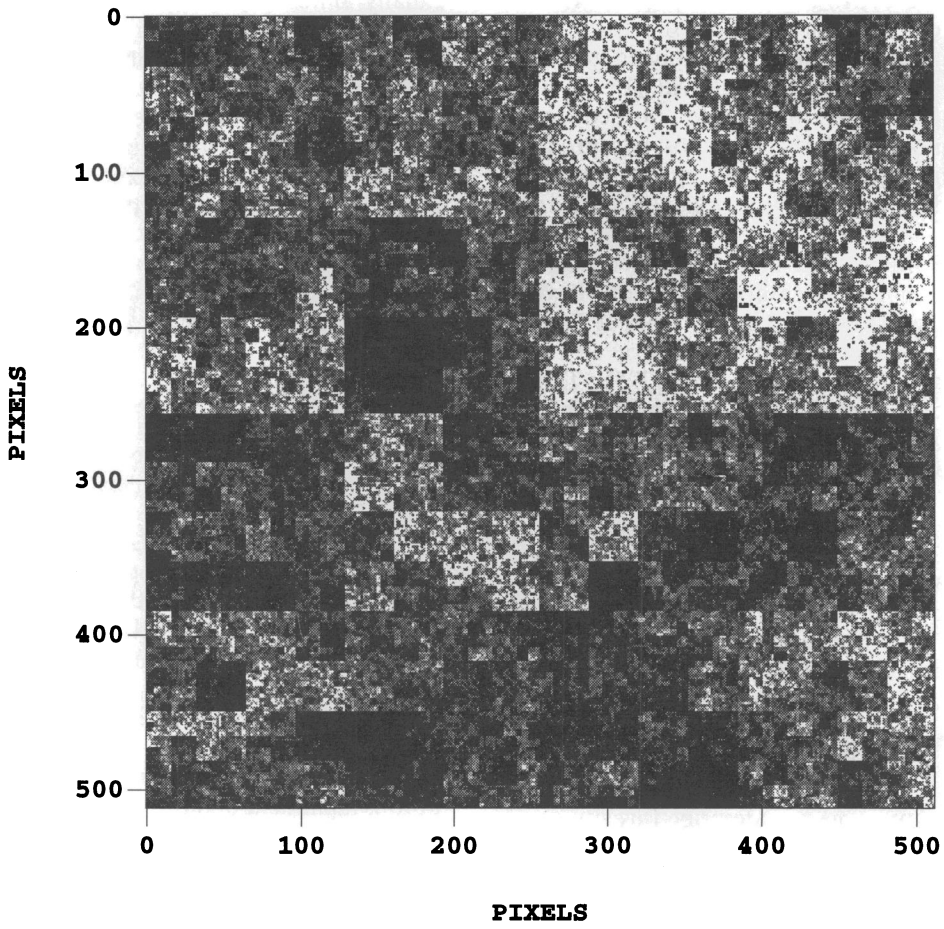

FIG. 1.—Gray-scale, 512 pixels × 512 pixels image constructed from the first nine steps of a multiplicative cascade procedure with a triangular distribution density. Black is low measure, white is high measure.

sions are directly related to these moments (Meneveau & Sreenivasan 1991; Chhabra & Sreenivasan 1991a, b; for a two-dimensional version see Lawrence et al. 1995a):

$$D_q = \frac{1}{(1-q)}\left[2 + \frac{2\ln\langle M^q\rangle}{\ln(2)}\right]. \quad (2.6)$$

Figure 2 shows as a solid line the analytical form of D_q. This gives $D_0 = 2$, in agreement with the fact that this measure fills its two-dimensional embedding space.

Also shown in Figure 2 are the results of a box counting calculation of D_q and $C(q)$ via equation (2.3) over the range 3 pixels $\leq s \leq$ 16 pixels and with 50,000 Monte Carlo samplings. $C(q)$ is zero within the error bars for $-0.5 < q < 5$, so there are no finite-size effects here. This expectation is borne out by the excellent fit of the box counting D_q to the analytical curve. The finite range of q over which the good fit occurs may be laid to the singularity of $\langle M^q\rangle$ at $q \leq -2$ and to the finite scaling range. In particular, the increasing scatter with $q > 2$ of the box counting values of D_q and $C(q)$ indicates the basic limit of accuracy that can be attained in a 512 pixels × 512 pixels image.

2.3. *Multifractional Spectrum*

Relabel the coarse-grained measure $\mu_i(\epsilon)$ in the ith box in terms of its coarse Hölder exponent α_i, where

$$\mu_i(\epsilon) = \epsilon^{\alpha_i}. \quad (2.7)$$

Because $\epsilon < 1$, large values of α correspond to small values of μ. For each ϵ, make a histogram of the number $dN(\alpha, \epsilon) = n(\alpha, \epsilon)d\alpha$ of boxes with "singularity strength" α in bins of width $d\alpha$. If the number density $n(\alpha, \epsilon)$ scales for $\epsilon \to 0$ according to

$$n(\alpha, \epsilon) \sim \phi(\ln\epsilon)\epsilon^{-f(\alpha)}, \quad (2.8)$$

with $f(\alpha)$ independent of ϵ, then the measure is multifractal according to the criteria of Evertsz & Mandelbrot (1992).

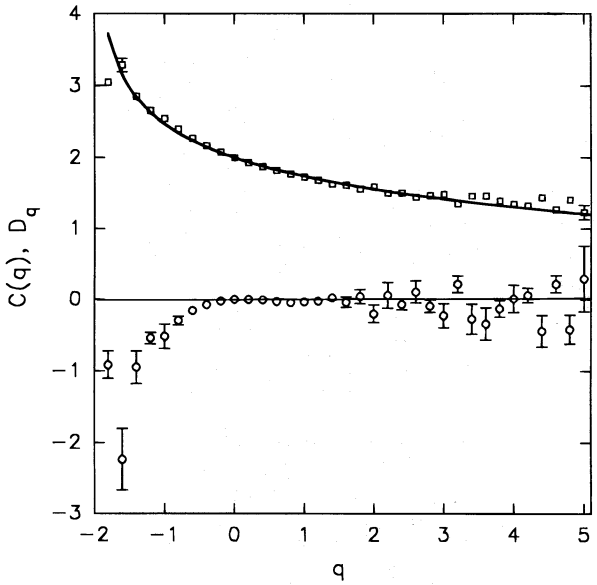

FIG. 2.—Analytical form (*solid line*) of D_q for the measure of Fig. 1. Box counting calculation of D_q (*squares*) and $C(q)$ (*circles*) for this measure over the range 3 pixels $\leq s \leq$ 16 pixels and with 50,000 Monte Carlo samplings. Error bars represent the precision of the linear fits. Those not shown on the box counting values are smaller than the symbols.

The "multifractal spectrum" $f(\alpha)$ amounts to a double logarithmic plot (to base ϵ) of the probability distribution of measure in the coarse-graining boxes.

Finiteness of the total measure in the limit $\epsilon \to 0$ requires that $f(\alpha)$ touch from below, but not cross, the bisector line $f(\alpha) = \alpha$. The scaling correction $\phi(\ln\epsilon)$ is required to conserve the measure for variable finite ϵ. We have used the form

$$\phi(\ln\epsilon) = C(\alpha)\left[\ln\left(\frac{1}{\epsilon}\right)\right]^{1/2}\left[1 + \frac{C_1}{\ln(1/\epsilon)} + \frac{C_2}{\ln^2(1/\epsilon)} + \cdots\right] \quad (2.9)$$

derived by van de Water & Schram (1988). The $+1/2$ exponent corrects typographical sign errors in equation (7) of Lawrence et al. (1993) and in equation (2.4) of Cadavid et al. (1994). $C(\alpha)$ is an undetermined function of α. While they are irrelevant asymptotically, the unknown constants C_n are important in a resolution-limited context. Thus, although we can establish multifractality in solar fields (Lawrence et al. 1993; Cadavid et al. 1994), ambiguity in the scaling correction leaves $f(\alpha)$ numerically inaccurate (Meneveau & Sreenivasan 1989; see also Lawrence et al. 1995a).

The derivation of equation (2.9) assumes that $f(\alpha)$ is tangent to the bisector at a point α_1, that it can be expanded in a Taylor's series about that point, and that the leading noncanceling term in the expansion of $h(\alpha) \equiv \alpha - f(\alpha)$ is the quadratic term proportional to $f''(\alpha_1)$. If, however, the second derivative vanishes, then the leading term will be proportional to some higher (even) derivative $f^{(n)}(\alpha_1)$. In this case the leading logarithmic factor becomes $[\ln(1/\epsilon)]^{1/n}$. If $f(\alpha)$ is in contact with the bisector over a finite range, the leading factor is $[\ln(1/\epsilon)]^0 = 1$. If, on the other hand, $f(\alpha)$ is not differentiable at α_1, but can be approximated as linear on either side of that point, then the leading factor becomes $[\ln(1/\epsilon)]^1$. As an alternate, more robust (and truncated), version of equation (2.9), we thus could adopt

$$\phi(\ln\epsilon) = C(\alpha)[\ln(1/\epsilon)]^{\beta}. \quad (2.10)$$

In what follows we will look at both forms to preserve continuity with earlier work.

The scaling correction $\phi(\ln\epsilon)$ is closely analogous to a scaling correction factor introduced by Scotti et al. (1995) for the fractal dimensions of graphs of functions. That correction also reflects the finite resolution of the series.

For a simple fractal, the multifractal spectrum collapses to the point $\alpha = f(\alpha) = D$. Under the condition $f''(\alpha) < 0 \Leftrightarrow dD_q/dq < 0$, the quantities $\alpha, f(\alpha)$, and the quantities q and $(q-1)D_q$ are formally equivalent and are connected by a Legendre transformation:

$$\alpha = \frac{d}{dq}[(q-1)D_q], \quad f(\alpha) = q\alpha - (q-1)D_q \quad (2.11)$$

(Frisch & Parisi 1985; Halsey et al. 1986). The maximum value $f_{\max}(\alpha) = D_0$.

Figure 3 shows as a dashed line the $f(\alpha)$ curve calculated by a Legendre transformation from the analytical D_q curve in Figure 2. Although the analytical D_q does not exist for $q \leq -2$, the transformation maps the point $q = 2$ to $\alpha = \infty$, $f(\alpha) = -\infty$, so the whole singularity spectrum remains present. For a classification of forms of multiplicative probability distribution densities and the singularities arising from them, see Hentschel (1994). The solid line in Figure 3 is

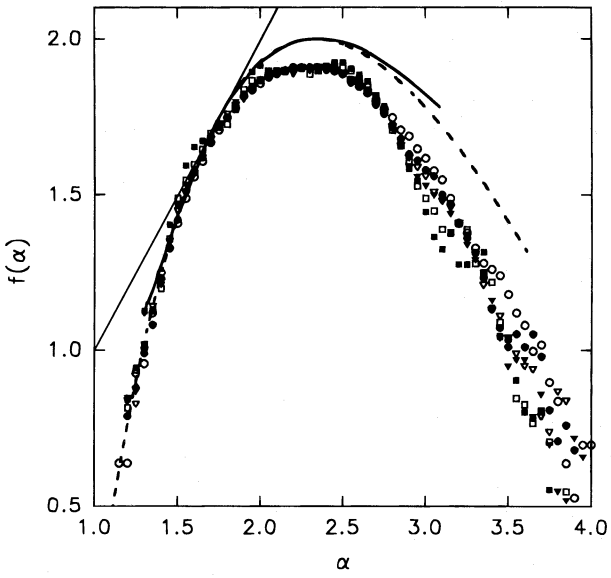

FIG. 3.—$f(\alpha)$ curve calculated by Legendre transformation from the analytical D_q curve in Fig. 2 (*dashed line*). The $f(\alpha)$ curve calculated by Legendre transformation from the box counting D_q in Figure 2 (*solid line*). The sets of symbols denote $f(\alpha, \epsilon)$ curves for box sizes 2 pixels (*open circles*), 3 pixels (*filled circles*), 4 pixels (*open triangles*), 6 pixels (*filled triangles*), 8 pixels (*open squares*), and 12 pixels (*filled squares*) calculated with the values $C(\alpha) = 1$ and $C_1 = -1.05$ and including 100,000 Monte Carlo samples.

calculated from the box counting D_q shown in Figure 2 and represents the case of resolution-limited asymptotics. These are in good agreement.

We also carry out a direct calculation of the $f(\alpha)$ curve by means of a resolution-limited asymptotic version of equation (2.8). First, we write this in the form

$$f(\alpha, \epsilon) = \frac{\ln [n(\alpha, \epsilon)/\phi(\ln \epsilon)]}{\ln (1/\epsilon)} . \qquad (2.12)$$

Next, $\phi(\ln \epsilon)$ is adjusted so that the $f(\alpha, \epsilon)$ curves for different ϵ are (1) congruent to the greatest extent possible and (2) tangent to the bisector. We have chosen to cut off the power series in equation (2.9) after the C_1 term, introducing an error $\sim(1/\ln L)^2$. We have associated the value of L with the size of our image, but the true value is unknown. $C(\alpha)$ and C_1 are treated as free parameters in meeting criteria (1) and (2). The sets of symbols in Figure 3 denote $f(\alpha, \epsilon)$ curves for box sizes $s = 2, 3, 4, 6, 8, 12$ pixels calculated with the values $C(\alpha) = 1$ and $C_1 = -1.05$ and including 100,000 Monte Carlo samplings. These coincide in the range $1.2 < \alpha < 2.8$, demonstrating scaling, and they are tangent to the bisector. However, they give $D_0 \approx 1.9$, too small by about 5%. This is attributable to truncation of the scale correction $\phi(\ln \epsilon)$. Use of the prefactor in equation (2.10) in place of that of equation (2.9) gives optimum parameter values $C(\alpha) = 0.8$ and $\beta = 0.3$. This leads to a plot of $f(\alpha, \epsilon)$ curves indistinguishable from that of Figure 3.

Lawrence et al. (1995a) have examined positive definite measures constructed from the square of the transverse gradients of line-of-sight fields in solar magnetic images. These measures show strong multifractal scaling. The multifractal spectrum was calculated as in the present case except that an observational determination of $P(M)$ was substituted for the analytical computation. This leads to a plot virtually identical to Figure 3.

Because of the form of equation (2.12), Tao et al. (1995) have mistaken our "curve matching" version of the histogram method for an erroneous division by $\ln(1/\epsilon)$ and advocate a standard linear fitting version instead. The situation is akin to finding the slope of a linear sequence of points in a two-dimensional plot. If the line through the points passes through the origin of coordinates, then we can find the slope by simply dividing the ordinates of the points by their abscissae. If the line does not pass through the origin we have two possibilities. On the one hand, we can carry out a linear fit to the points, determining both the slope and the intercept. On the other hand, we can move the origin of coordinates [by choosing $C(\alpha)$ and C_1, or $C(\alpha)$ and β] to meet the line through the points and *then* divide the ordinates by the abscissae. Our curve matching approach is analogous to the second choice and is fully valid, as is its application in Lawrence et al. (1993). This is explored further for an image from that paper in the next subsection.

We point out additionally that Tao et al. (1995) were commenting on the generalized dimension approach to multifractal scaling, rather than the direct calculation of $f(\alpha)$ we have used. This second approach is preferrable for analysis of real, observational data, because it shows the quality of the data and degree of scaling very directly. The generalized dimensions, however, are calculated by averaging moments of the measure over the whole image, and this introduces a sometimes misleading appearance of regularity to the result.

2.4. *Scaling of a Solar Magnetic Image*

Figure 4 is a line-of-sight magnetic field image of NOAA active region 5643 made under good seeing conditions with the San Fernando Observatory video spectra–spectroheliograph system on 1989 August 17. The pixel scale is 0".46 pixels^{-1}, and the field of view is 480 pixels east-west and 550 pixels north-south. Resolution is seeing limited at >1". This image was studied in Lawrence et al. (1993); here we compare the curve matching and standard fitting calculations of $f(\alpha)$.

Figure 5 shows D_q and $C(q)$ for this signed measure. We have seen in § 2.2 that they do not exist for $q \leq -1$. For $0 \leq q \leq 3$, $D_q = D \approx 2$ resembles a simple fractal. For $q > 3$, D_q begins to decrease slowly. The $C(q)$ curve indicates the presence of finite-size effects.

Because the Legendre transformation is ineffective here, we rely on the histogram method to calculate $f(\alpha)$. Figure 6 shows $f(\alpha, \epsilon)$ curves for $s = 2, 3, 4, 6, 8, 12$ pixels and the choices $C(\alpha) = 1.2$, $C_1 = -1.4$. These display scaling over the range $1.7 \leq \alpha \leq 2.2$. The structures at $\alpha > 2.2$ are analytically treatable finite-size effects of the image noise (Cadavid et al. 1994). Again, $f_{\max}(\alpha) = D_0 = 1.9$ is too small by $\sim 5\%$, because we have truncated equation (2.9) after the C_1 term. Finally, use of the equation (2.10) prefactor gives no discernable improvement in the matching of the $f(\alpha, \epsilon)$ curves, but leads to the parameter values $C(\alpha) = 0.5$ and $\beta = 0$. This last value is not surprising, since the $f(\alpha, \epsilon)$ curves appear to follow the bisector over a finite range.

The scaling of $f(\alpha)$ seen in Figure 6 is obtained by assuming that both $\ln [n(\alpha, \epsilon)/\phi]$ and $\ln \mu$ vary linearly with $\ln \epsilon$. To check this, we define $X(\epsilon) \equiv \ln \mu(\epsilon)$. $X(\epsilon)$ varies between some $X_{\min}(\epsilon)$ and $X_{\max}(\epsilon)$, and at each scale we follow the procedure suggested by Meneveau & Sreenivasan (1989) by dividing this range into 20 equal intervals of size ΔX and checking the scaling for each interval. Box counting is implemented for 600 realizations of a fixed

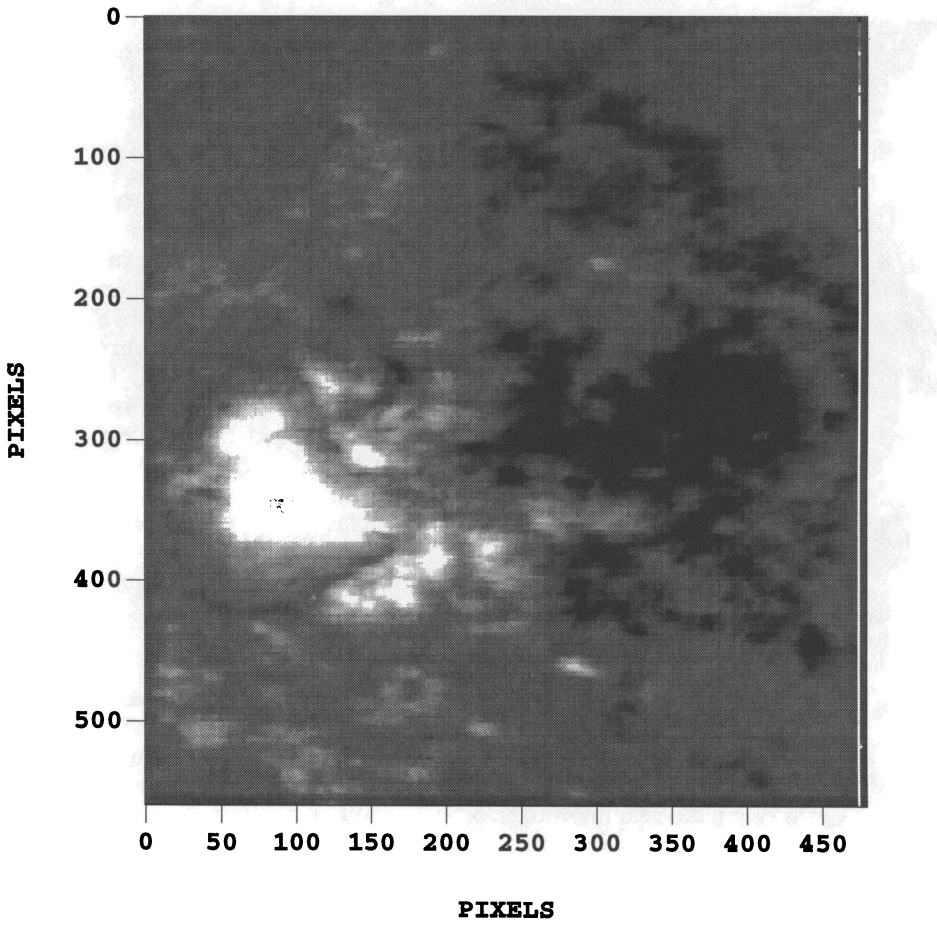

FIG. 4.—Line-of-sight magnetic field image of NOAA active region 5643 made under good seeing conditions with the San Fernando Observatory video spectra–spectroheliograph system on 1989 August 17. The pixel scale is 0.″46 pixel^{-1}, and the field of view is 480 pixels east-west and 550 pixels north-south. Resolution is seeing limited at >1.″

course-graining grid with location varied randomly by up to 32 pixels in rows and columns. Figure 7 shows the linear scaling of ln $\mu_i(\epsilon)$ versuls ln (ϵ) for six of the 20 intervals. The scaling range is 5–30 pixels. The slopes of the lines are the corresponding α_i. It is clear that the linear fits are especially good for $1.6 \leq \alpha \leq 2.17$, verifying that the *Ansatz* of equation (2.7) is physically realistic. For $\alpha > 2.17$, corresponding to weaker magnetic fields, the fits are degraded, probably by the effects of image noise (see Fig. 6). This effect also was observed for turbulent motions of the terrestrial atmosphere (Meneveau & Sreenivasan 1989), and the same interpretation was placed upon it. Figure 8 shows plots of ln $[n(\alpha, \epsilon)/\phi(\ln \epsilon)]$ versus ln ϵ for six values of α. For convenience, we have chosen data points from bins equally spaced in α. The prefactor $\phi(\ln \epsilon)$ uses $C = 1.2$ and $C_1 = -1.4$. The scaling range is 4–28 pixels. Once again, we see good linear fits; the slopes give $-f(\alpha_i)$. The filled circles with error bars in Figure 6 show the $f(\alpha)$ curve obtained by linear fitting over the range 2–12 pixels. For $1.7 \leq \alpha \leq 2.2$, this agrees closely with the curve matching plots. However, for $2.2 < \alpha < 2.6$, the fitted curve is too high, even extending above $D_0 = 2$. For $s \geq 2.6$, the fitted curve is too low. These excursions are due to image noise. While the standard fitting method blindly calculates a value for $f(\alpha)$, the curve matching procedure points clearly to the influence of two distinct phenomena: the scaling of the magnetic flux and the presence of image noise.

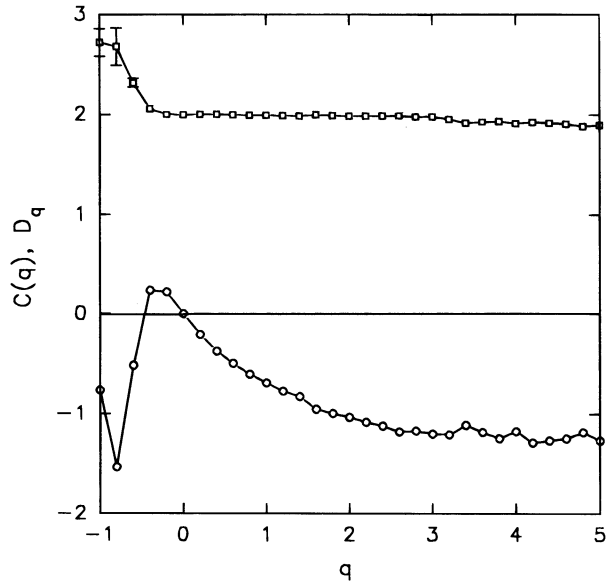

FIG. 5.—D_q (*squares*) and $C(q)$ (*circles*) for the signed measure of Fig. 4

3. DIMENSIONS OF SIMPLE FRACTALS

For simple fractals, all elements of the fractal set have the same measure μ_0.

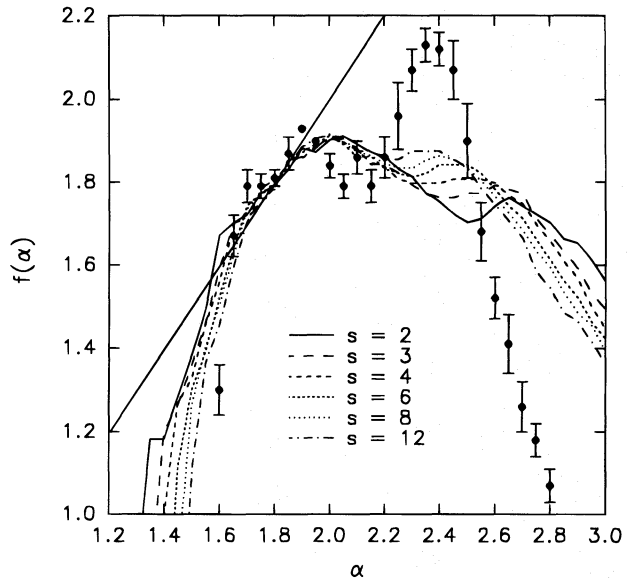

FIG. 6.—$f(\alpha, \epsilon)$ curves for $a = 2$, 3, 4, 6, 8, 12 pixels and the choices $C(\alpha) = 1.2$, $C_1 = -1.4$. Filled circles with error bars represent the $f(\alpha)$ curve obtained by linear fitting over the range 2–12 pixels. The solid line is the bisector $f(\alpha) = \alpha$.

3.1. *Box Counting Dimension*

Cover the image with a grid of coarse-graining boxes of uniform scale $\epsilon \ll 1$. If $N(\epsilon)$ is the number of boxes containing any measure, then the asymptotic limit

$$D = \lim_{\epsilon \to 0} \frac{\ln N(\epsilon)}{\ln (1/\epsilon)} \tag{3.1}$$

is defined to be the fractal dimension of the supporting set of the measure. For data, the asymptotic limit is unavailable, so we seek a resolution-limited asymptotic scaling range between the inner and outer cutoffs. For finite size boxes in this range, $N(\epsilon) \propto \epsilon^{-D}$ and

$$\ln N(\epsilon) = C + D \ln (1/\epsilon) , \tag{3.2}$$

where C is a constant intercept fixed by linear fit of $\ln N(\epsilon)$ to $\ln (1/\epsilon)$. In analyzing the fractal properties of data, the difference between these two definitions of D is crucial. Discrepancies between the two for the dimensions of graphs of time series are discussed in detail by Scotti et al. (1995).

An instructive test example starts with a measure uniformly distributed on a square, divides the square into four equal quarters, and distributes the measure evenly in three of them chosen at random. The process is repeated for each of the filled subsquares, then all of the filled subsubsquares, and so on to infinity. Figure 9 is a 512 pixels × 512 pixels realization of this process through the first nine levels of partition. At the nth level of this process, the set consists of 3^n filled pixels in a square 2^n pixels on a side. Thus, the fractal dimension is $D = \ln 3/\ln 2 \approx 1.585$.

Let us determine the fractal dimension in the resolution-limited asymptotic regime. Figure 10 shows $\ln N(q, \epsilon)$ versus $\ln (1/s) = \ln (1/\epsilon) + \text{constant}$ for the case $q = 0$. $N(0, \epsilon) \equiv N(\epsilon)$, the unweighted number of boxes described above. The slope is not constant over the full range 1 pixel $\leq s \leq 64$ pixels but shows a break at $s \approx 6$ pixels. Over 1 pixel $\leq s \leq 6$ pixels, a rough linear fit gives $D = 1.30 \pm 0.03$, clearly too small. For 6 pixels $\leq s \leq 64$ pixels, the fit gives $D = 1.627 \pm 0.006$, which is too large.

What has gone wrong? Unless they match the original cascade partitioning, both in size and location, our coarse-graining boxes will contain varying amounts of measure $\mu \leq \mu_0$ and so cannot cover the fractal set efficiently. Thus, when $s > 1$ pixel, the number of boxes counted will be too large. However, for $s = 1$ pixel, the boxes must match the partitioning and the correct number of boxes will be counted; hence, the curvature in the plot. The situation can be improved by weighting each box in the sum by a power $q > 0$ of the amount of measure it contains: we calculate a generalized dimension D_q for $q > 0$. These would be independent of q in the asymptotic limit, but in the resolution-limited asymptotic case, values of $q > 1$ cover the set more precisely and give better results. Figure 10 also shows $\ln N(q, \epsilon)$, where $N(q, \epsilon)$ is the weighted number of boxes, versus $\ln (1/s)$ for $q = 8$. The plot is linear over 1 pixel $\leq s \leq 64$ pixels and yields $D_8 = 1.572 \pm 0.004$, a better approximation to the asymptotic value.

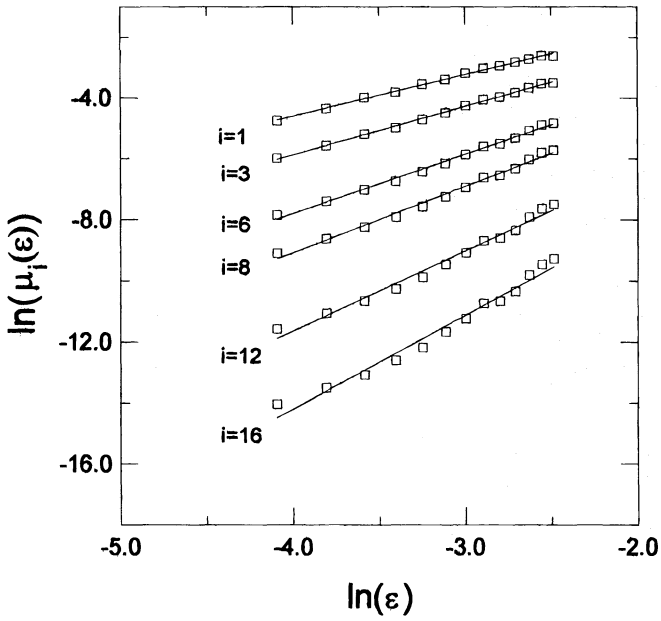

FIG. 7.—Linear scaling of $X(\epsilon) = \ln \mu_i(\epsilon)$ vs. $\ln \epsilon$ for selected intervals $\Delta X(\epsilon)$. The scaling range is 5–30 pixels. The slopes of the lines are the corresponding α_i.

3.2. *Cluster Dimension*

A different kind of dimension has been studied by a number of groups. Discrete clusters of pixels in a fractal set can represent granules (Brandt et al. 1991) or magnetic plages (Balke et al. 1993). A fractal dimension governs the scaling of the number of pixels A (the "area" or "mass") with the linear size L of each cluster:

$$A \propto L^{D_{cl}} . \tag{3.3}$$

In practice, D_{cl} is the slope of a plot of $\ln A$ versus $\ln L$.

Figure 11 is a 256 × 256 array of pixels that are randomly occupied or not with probability $p = 0.5$. The occupied pixels are black (an arbitrary choice in this case). Clusters are defined by continuous sets of occupied nearest neighbor pixels, and percolation theory (Stauffer & Aharony 1992) indicates $D_{cl} = 1.56$ for such clusters. We have identified 278 discrete clusters in Figure 11, with linear size restricted

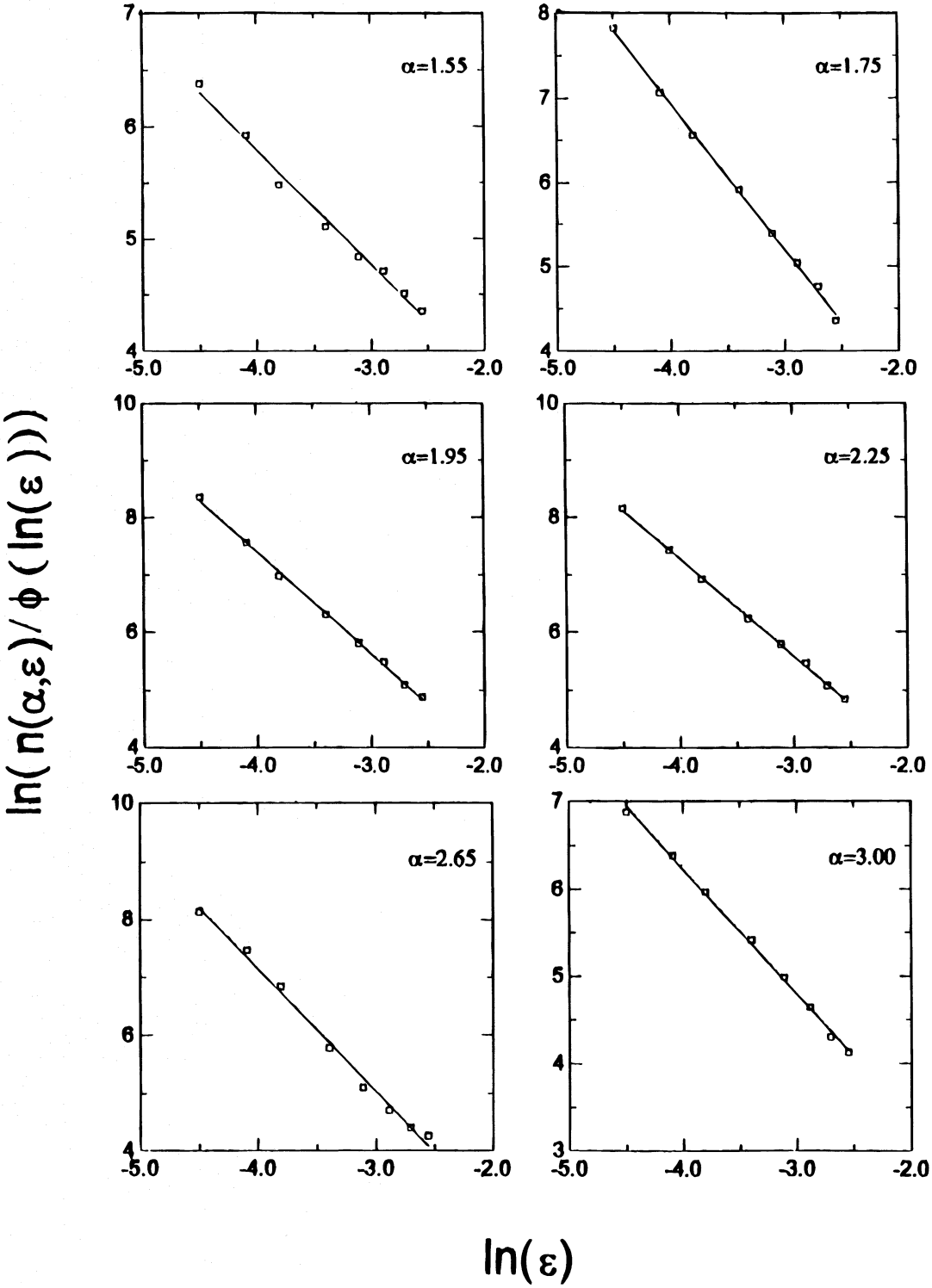

FIG. 8.—ln $[n(\alpha, \epsilon)/\phi(\ln \epsilon)]$ vs. ln ϵ for six values of α

for convenience to 10 pixels or more. Figure 12 is a log-log plot of the areas versus the sizes; the linear fit gives $D_{cl} = 1.54 \pm 0.04$, in agreement with percolation theory. The box counting dimension of the set of occupied pixels, however, is $D = 2$.

3.3. *Threshold Sets*

A "threshold dimension" D_{th} is the fractal dimension of the support (the "threshold set") of that portion of a positive definite measure lying above some given value. If the threshold value is zero, $D_{th} = D_0$. From the asymptotic nature of the information theoretic dimension D_1 in equation (2.2), however, it follows that for any threshold level greater than zero, $D_{th} = D_1$ (Farmer, Ott, & Yorke 1983). Does this hold for resolution-limited asymptotics? For the known multifractal measure of § 2.1, the analytical $D_1 = 1.740$. Tao et al. (1995) prescribe that D_{th} be taken to be D_0 of the threshold set calculated via equation (3.2). As we have

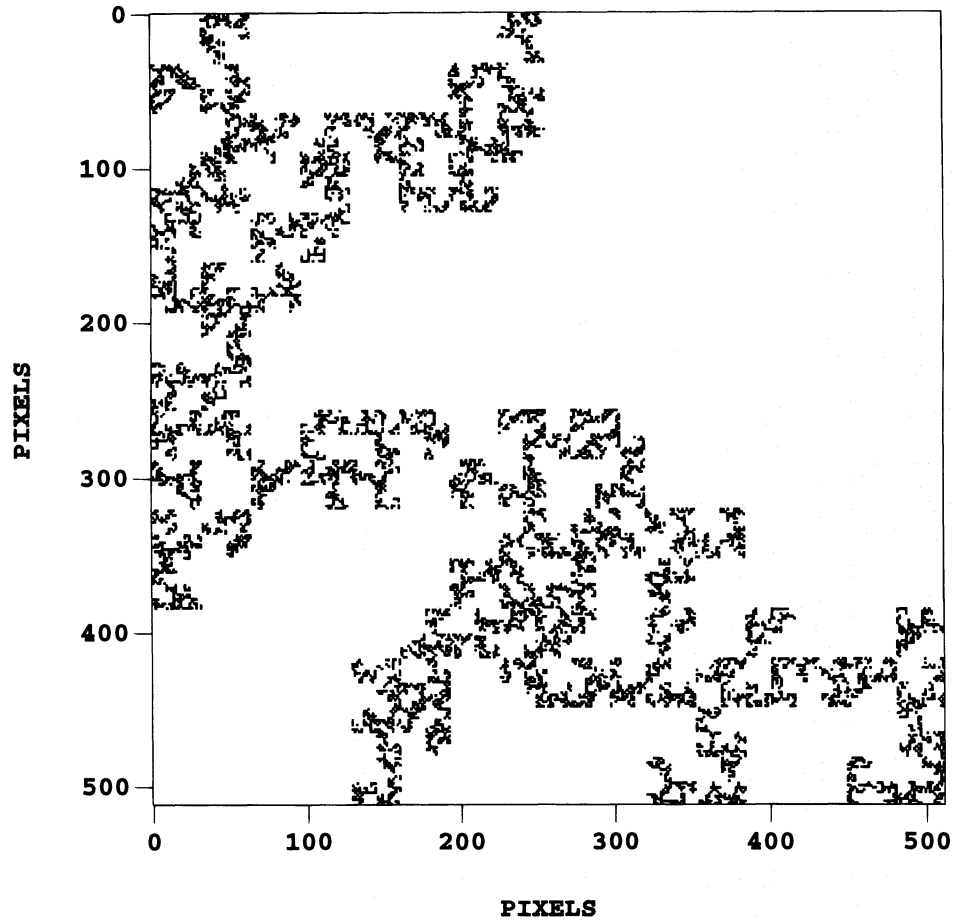

FIG. 9.—512 pixels × 512 pixels realization of the first nine levels of a partition that distributes the measure in a square equally among three of its quarters. The fractal dimension is $D = \ln 3/\ln 2 \approx 1.585$.

seen in § 3.1, however, coarse-graining boxes cannot cover such black-and-white sets efficiently, and workers who follow this prescription are likely to obtain incorrect results. We again use D_q and arbitrarily choose $q = 8$ (still not a perfect procedure). If the threshold level is such that the lowest 4% of the measure is excluded, we find $D_{th} = 1.907 \pm 0.005$, if 17% is excluded, $D_{th} = 1.815 \pm 0.005$, and if 42% is excluded, $D_{th} = 1.63 \pm 0.02$. For resolution-limited asymptotics, D_{th} is strongly dependent on the threshold level and therefore $\neq D_1$. Tao et al. (1995) have found a closer coincidence between D_{th} and D_1 for a simulated magnetic image. The preceding discussion suggests that this result is fortuitous.

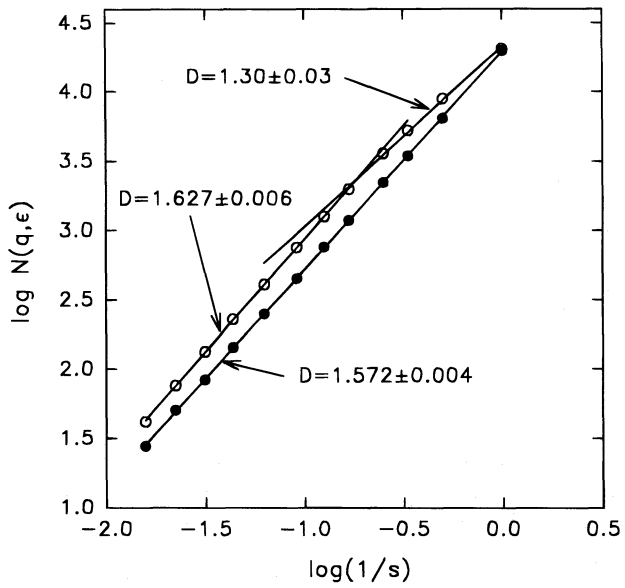

FIG. 10.—Log-log plot of $N(q, \epsilon)$ vs. $1/s$ over the range 1 pixel $\leq s \leq 64$ pixels for $q = 0$ (*open circles*) and $q = 8$ (*filled circles*) for the fractal set of Fig. 9.

3.4. *An Observational Example*

Figure 13 is constructed from a Lockheed–La Palma magnetogram of plage in NOAA active region 5168 on 1988 September 29 made with the Vacuum Tower Telescope of the Swedish Solar Observatory (Title et al. 1989). The spatial resolution in this image is $\sim 0''.5$, and the pixel scale is $0''.14$. The threshold set includes those pixels with $|B_{||}| \geq 500$ G. This threshold matches the analysis of the same image by Balke et al. (1993). Figure 14 is a log-log plot of $N(q, \epsilon)$ versus $1/s$ over the range 1 pixel $\leq s \leq 64$ pixels for $q = 0$ and $q = 8$. As before, $q = 0$ gives greater values of N, but now the $q = 8$ plot shows a break at $s \approx 11$ pixels. For $s \leq 11$ pixels, $D_8 = 1.90 \pm 0.01$. At the smallest scales, the threshold set in Figure 13 is made up of almost–two-dimensional objects. This is a consequence of the image resolution and the sizes of magnetic features at the 500 G level. For 16 pixels $\leq s \leq 64$ pixels, $D_8 = 1.54 \pm 0.04$, and $D_0 = 1.58 \pm 0.01$. We take these values as indicative of the actual fractal dimension.

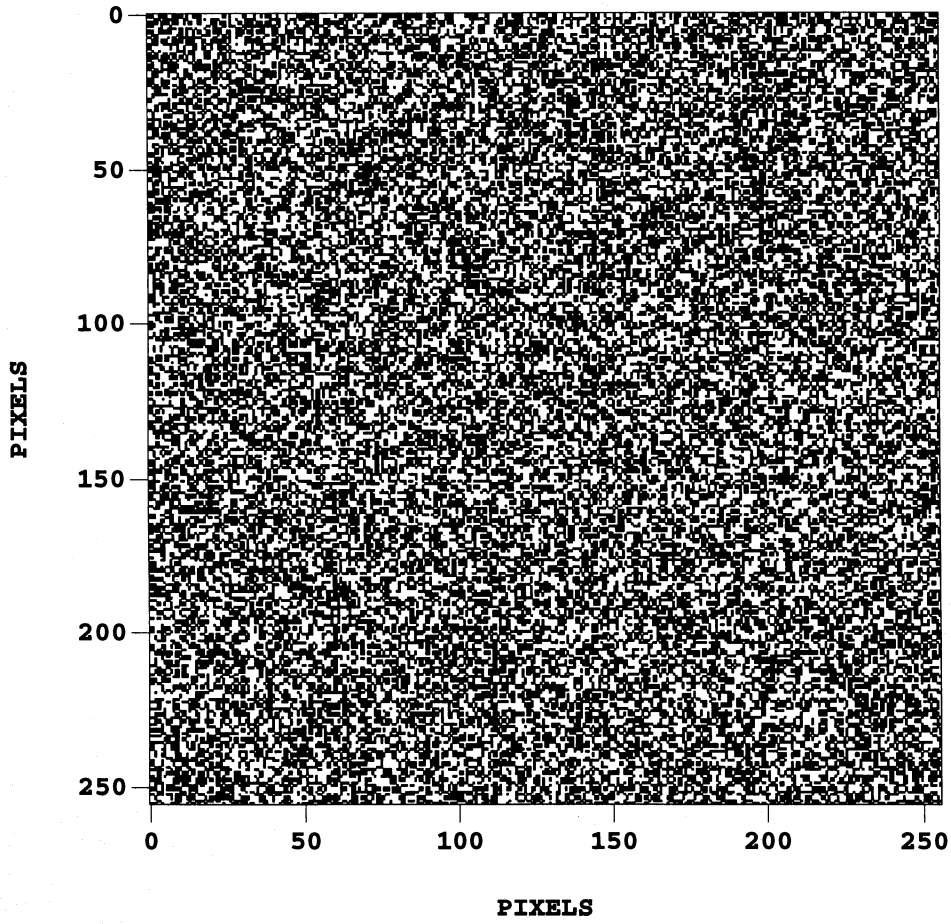

FIG. 11.—256 × 256 array of pixels that are randomly occupied (*black*) or not (*white*) with probability $p = 0.5$

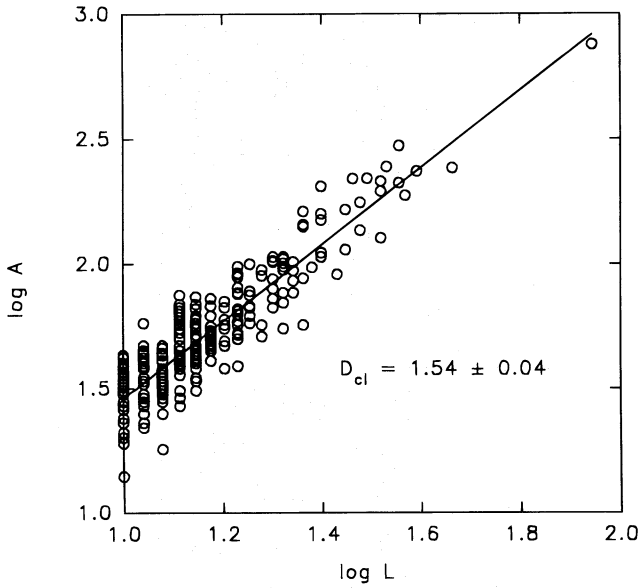

FIG. 12.—Log-log plot of cluster areas (masses) vs. linear size for the occupied set of Fig. 11.

The absolute value of the line-of-sight field in the original Lockheed–La Palma image from which Figure 13 was derived has a measure theoretic dimension of $D_1 = 1.844 \pm 0.007$ for scales $s \geq 8$ pixels. However, we found the fractal dimension of the threshold set at 500 G to be $D_{th} \approx 1.55 \neq D_1$.

We identify 67 discrete clusters in Figure 13 with linear size greater than 10 pixels. Figure 15 is a log-log plot of the cluster areas versus linear size and gives $D_{cl,} = 1.75 \pm 0.05$, virtually identical to the result of Balke et al. (1993). After numerical enhancement of the resolution, Tarbell et al. (1990) estimated $D_{cl} \approx 1.6$, and Balke et al. (1993) found $D_{cl} = 1.54 \pm 0.05$ for cluster sizes below the connectedness length. Because this smaller value coincides with that of the fractal dimension found in the preceding paragraph, it is tempting to identify these dimensions with one another. However, calculation of D_{cl} and D, using the threshold set exactly as it is in Figure 13 in each case, gives differing results. Further, the value of D refers to scales $> 5''$, while to obtain the lower value of D_{cl} we must go to scales an order of magnitude smaller.

Tao et al. (1995) have suggested an obvious connection

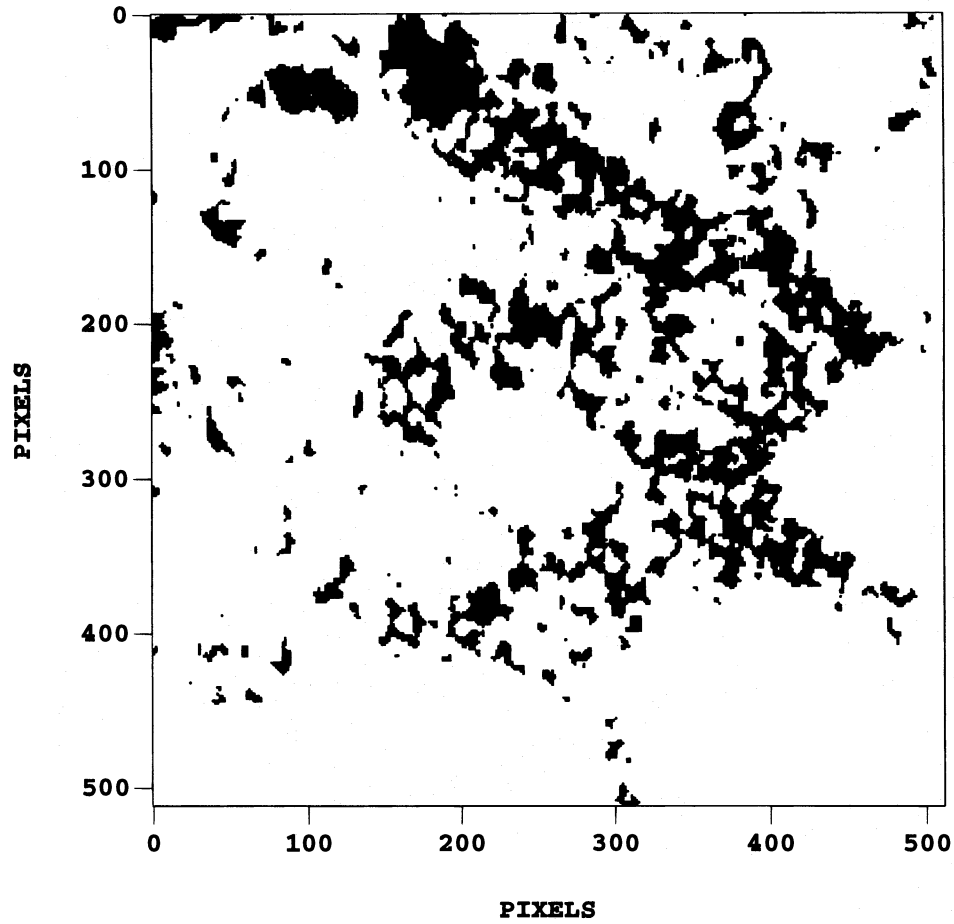

FIG. 13.—Threshold set constructed from a Lockheed–La Palma magnetogram of plage in NOAA active region 5168 on 1988 September 29 made with the Vacuum Tower Telescope of the Swedish Solar Observatory (Title et al. 1989). The spatial resolution in this image is ~0".5, and the pixel scale is 0".14. The threshold set includes those pixels (*black*) with $|B_{||}| \geq 500$ G.

between D_{cl} and D_{th}. This is not present in resolution-limited asymptotics. Aside from differing numerical values, the two dimensions have different meanings. On the one hand, the cluster dimension refers to the scaling of the masses versus linear sizes of the individual clusters, where all are measured at the finest, single pixel level. The threshold dimension, on the other hand, refers to the scaling of the mass of the whole field of clusters versus the variable coarse-graining level at which it is measured.

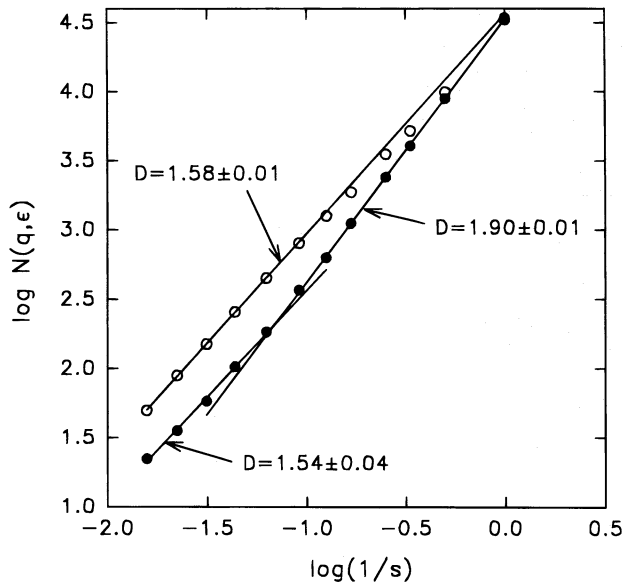

FIG. 14.—Log-log plot of $N(q, \epsilon)$ vs. $1/s$ over the range 1 pixel $\leq s \leq 64$ pixels for $q = 0$ (*open circles*) and $q = 8$ (*filled circles*) for the threshold set of Fig. 13.

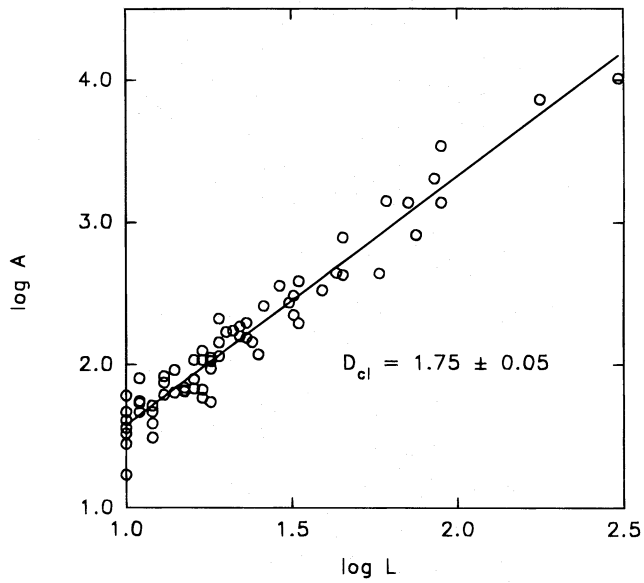

FIG. 15.—Log-log plot of cluster areas (masses) versus linear size for the set of Fig. 13

4. DISCUSSION

The point of departure for this paper has been the crucial difference between the asymptotic, mathematical definitions of fractal quantities and the versions of these quantities one can expect to calculate from real data. For example, the threshold dimension theorem of Farmer et al. (1983), though valid in the asymptotic limit, does not manifest itself in resolution-limited asymptotics.

The histogram approach to calculating $f(\alpha)$ spectra is complicated by the necessity of undetermined scaling corrections that arise from finite resolution, Although this method is therefore numerically inaccurate, it is convenient as a test for the presence of multifractal scaling. It has the further advantage of displaying the data directly, whereas the approach of averaging moments of the data introduces an artificial smoothing of the results. We have compared the utility of two formally equivalent techniques for this calculation, which we have called the "curve matching" procedure and the standard linear fitting. The latter requires a separate fit for each value of α. Curve matching allows us to choose a simplified form of the intercept, in particular $C(\alpha) =$ contant in equation (2.9), and so to demonstrate convergence of the $f(\alpha)$ with only one computation. Further, the detailed behavior of the $f(\alpha, \epsilon)$ in different parts of the spectrum (e.g., congruence for $1.7 < \alpha < 2.2$, a characteristic divergence for $\alpha > 2.2$) are plainly visible for curve matching and aid in physical interpretation. While the fitting method blindly calculates values for $f(\alpha)$, the curve matching procedure exposes two distinct phenomena in the image: the scaling of the magnetic flux and the presence of noise (see Fig. 6).

Box counting measurements of dimensions of simple fractals, or of multifractals that do not fill their embedding space (with $D_0 < 2$), are unreliable in the resolution-limited asymptotic regime. This is a consequence of the inability of coarse-graining boxes to cover the supporting sets efficiently. A partial cure is to use D_q for higher values of q, so as to weight the count of boxes according to the amount of measure they contain. As can be seen in Figure 2, box counting works well for a multifractal that does fill its embedding space. Here every sample box covers something.

We have compared cluster and threshold dimensions in the resolution-limited asymptotic regime. Aside from differing numerical values, the two dimensions have different meanings. On the one hand, the cluster dimension refers to the scaling of the masses versus linear sizes of the individual clusters, where all are measured at the finest, single pixel level. The threshold dimension, on the other hand, refers to the scaling of the mass of the whole field of clusters versus the variable coarse-graining level at which it is measured. D_{cl} does not refer to the geometrical location of one cluster relative to another. Schrijver (1994) has also indicated the difference between cluster and box counting dimensions of sets. Certainly the fractal set of Figure 10 provides a strong counterexample to their equality. In this particular case, the clusters are tightly intertwined and the two approaches give very different results. The fractal set in Figure 12 is more loosely structured, but when calculated at the resolution shown there the two dimensions differ ($D_{cl} = 1.75 \pm 0.05$ and $D \approx 1.55$). The cluster dimension is related to the fractal dimension $D_{rw} = 1.56 \pm 0.05$ inferred from the random walks of magnetic elements on the Sun (Lawrence & Schrijver 1993). Here each walker is confined to its own single cluster. The measured value of D_{rw} suggests a connection to random clusters like those in Figure 10 below percolation threshold (Schrijver et al. 1992).

The application of fractal and multifractal ideas to solar problems is an expanding enterprise. It is natural to expect, as workers familiarize themselves with new concepts, that confusion and misunderstanding will occur. It is hoped that the examples presented here will help to clarify the relationships among the work of different groups and will facilitate development of these powerful techniques.

The authors thank the two anonymous referees, whose comments have brought about significant improvement in this paper. A. C. C. acknowledges released time provided by the CSUN Research and Grants Committee. This work was supported in part by NSF grants ATM-9115111 and ATM-9309901.

REFERENCES

Balke, A. C., Schrijver, C. J., Zwaan, C., & Tarbell, T. D. 1993, Sol. Phys., 143, 215
Brandt, P. N., Greimel, R., Guenther, E., & Mattig, W. 1991, in Applying Fractals in Astronomy, ed. A. Heck & J. M. Perdang (Berlin: Springer), 77
Cadavid, A. C., Lawrence, J. K., Ruzmaikin, A. A., & Kayleng-Knight, A. 1994, ApJ, 429, 391
Chhabra, A. B., & Sreenivasan, K. R. 1991a, Phys. Rev. A, 43, 1114
———. 1991b, in New Perspectives in Turbulence, ed. L. Sirovich (Springer: Berlin), 24
Dubuc, B., Zucker, S. W., Tricot, C., Quiniou, J. F., & Wehbi, D. 1989, Proc. R. Soc. London A, 425, 113
Evertsz, C. J. G., & Mandelbrot, B. B. 1992, in Chaos and Fractals: New Frontiers in Science, ed. H.-O. Peitgen, H. Jürgens, & D. Saupe (Berlin: Springer), 921
Farmer, J. D., Ott, E., & Yorke, J. A. 1983, Physica D, 7, 153
Frisch, U., & Parisi, G. 1985, in Turbulence and Predictability in Geophysical Fluid Dynamics, ed. M. Gil, R. Benzi, & G. Parisi (Amsterdam: North-Holland), 84
Grassberger, P. 1983, Phys. Lett., 97A, 227
Halsey, T. C., Jensen, M. H., Kadanoff, L. P., Procaccia, I., & Shraiman, B. I. 1986, Phys. Rev. A, 33, 1141
Hentschel, H. G. E., & Procaccia, I. 1983, Physica, 8D, 435
———. 1994, Phys. Rev. E, 50, 243
Lawrence, J. K. 1991, Sol. Phys., 135, 249
Lawrence, J. K., Cadavid, A. C., & Ruzmaikin, A. A. 1995a, Phys. Rev. E, 51, 316
———. 1995b, ApJ, 455, 366
Lawrence, J. K., Ruzmaikin, A. A., & Cadavid, A. C. 1993, ApJ, 417, 805
Lawrence, J. K., & Schrijver, C. J. 1993, ApJ, 411, 402
Meneveau, C., & Sreenivasan, K. R. 1989, Phys. Lett. A, 137, 103
———. 1991, J. Fluid Mech., 224, 429
Milovanov, A. V., & Zelenyi, L. M. 1993, Phys. Fluids B, 5, 2609
Ruzmaikin, A. A., Sockoloff, D., & Tarbell, T. 1991, in The Sun and Cool Stars: Activity, Magnetism, Dynamos, ed. I. Tuominen, D. Moss, & G. Rüdiger (Berlin: Springer), 140
Schrijver, C. J. 1994, in Solar Surface Magnetism, ed. R. J. Rutten & C. J. Schrijver (Dordrecht: Kluwer), 271
Schrijver, C. J., Zwaan, C., Balke, A. C., Tarbell, T. D., & Lawrence, J. K. 1992, A&A, 253, L1
Scotti, A., Meneveau, C., & Saddoughi, S. G. 1995, Phys. Rev. E, 51, 5594
Stauffer, D., & Aharony, A. 1992, Introduction to Percolation Theory (London: Taylor & Francis)
Tao, L., Du, Y., Rosner, R., & Cattaneo, F. 1995, ApJ, 443 434
Tarbell, T., Ferguson, S., Frank, Z., Shine, R., Title, A., Topka, K., & Scharmer, G. 1990, in Solar Photosphere: Structure, Convection, and Magnetic Fields, ed. J. O. Stenflo (Dordrecht: Kluwer), 147
Title, A. M., Tarbell, T. D., Topka, K. P., Ferguson, S. H., Shine, R. A., & the SOUP Team. 1989, ApJ, 336, 475
van de Water, W., & Schram, P. 1988, Phys. Rev. A, 37, 3118.